ADVANCED FUNCTIONAL MATERIALS
www.afm-journal.de

Conjugated Polythiophene Frameworks as a Hole-Selective Layer on Ta_3N_5 Photoanode for High-Performance Solar Water Oxidation

Jin Wook Yang, Hee Ryeong Kwon, Su Geun Ji, Jaehyun Kim, Sol A Lee, Tae Hyung Lee, Sungkyun Choi, Woo Seok Cheon, Younhwa Kim, Jungwon Park, Jin Young Kim, and Ho Won Jang**

Discovering a competent charge transport layer promoting charge separation in photoelectrodes is a perpetual pursuit in photoelectrochemical (PEC) water splitting to achieve high solar-to-hydrogen (STH) conversion efficiency. Here, a conjugated polythiophene framework (CPF-TTB) on Ta_3N_5 is elaborately electropolymerized, substantiating the hole transport behavior in their heterojunction. Tailored band structures of the CPF-TTB/Ta_3N_5 reinforce the separation of photogenerated carriers, elevating a fill factor of the photoanode modified with a cocatalyst. The enhanced hole extraction enables the $NiFeO_x$/CPF-TTB/Ta_3N_5/TiN photoanode to generate a remarkable water oxidation photocurrent density of 9.12 mA cm^{-2} at 1.23 V versus the reversible hydrogen electrode. A tandem device combining the photoanode with a perovskite/Si solar cell implements an unbiased solar water splitting with a STH conversion efficiency of 6.26% under parallel illumination mode. This study provides novel strategies in interface engineering for metal nitride-based photoelectrodes, suggesting a promise of the organic–inorganic hybrid photoelectrode for high-efficiency PEC water splitting.

1. Introduction

Artificial photosynthesis harnessing sunlight to convert into sustainable fuels holds immense potential to revolutionize the global energy landscape in the face of environmental crisis.[1,2] Photoelectrochemical (PEC) water splitting is a fundamental artificial photosynthesis process for hydrogen fuel production with zero carbon footprint.[3–6] However, the sluggish kinetics of water oxidation, which requires four electrons per oxygen molecule,[7,8] necessitates the development of advanced photoanodes to enhance the quantum efficiency of the PEC cell. Photoanodes have been developed by three main approaches: reducing a band gap of photon absorber for sufficient light harvesting, reinforcing the separation of photogenerated carriers for high fill factor (FF), and expediting surface reaction kinetics for cathodic onset potential.

Tantalum nitride (Ta_3N_5) has emerged as one of the most promising photoanode materials due to its narrow band gap of 2.1 eV and suitable band edge positions straddling water redox potentials.[9,10] In terms of the aforementioned light harvesting, Ta_3N_5 has a high theoretical photocurrent density of 12.9 mA cm^{-2} by extending light absorption into the visible spectrum, corresponding to a theoretical solar-to-hydrogen (STH) conversion efficiency of 15.9%.[11] However, the short hole diffusion length (≈50 nm) and the high surface state density of Ta_3N_5 cause recombination losses along the charge carrier pathway.[12,13] The poor carrier mobility not only limits its photocurrent density far below the theoretical value but also reduces the photovoltage, lowering the overall fill factor of the photoanode. Various strategies have been employed to interface engineering to improve the charge transport of Ta_3N_5: reducing surface states by passivation layers (TiO_x,[14] AlO_x[15]), enhancing interband hole extraction through transport layers (GaN,[16] Mg:GaN,[17] $BaTaO_2N$,[18] $SrTaO_2N$[19]), and delaying charge recombination by hole storage layers (Fh[20,21]). There is also defect engineering that improves carrier mobility within the photoanode through doping, such as Mg:Ta_3N_5,[22,23] Zr:Ta_3N_5,[24] La:Ta_3N_5,[25] and Ba:Ta_3N_5.[26,27] Among them, for the hole transport layer (HTL), the inorganic

J. W. Yang, H. R. Kwon, S. G. Ji, J. Kim, S. A Lee, T. H. Lee, S. Choi, W. S. Cheon, J. Y. Kim, H. W. Jang
Department of Materials Science and Engineering
Research Institute of Advanced Materials
Seoul National University
Seoul 08826, Republic of Korea
E-mail: jykim.mse@snu.ac.kr; hwjang@snu.ac.kr

Y. Kim, J. Park
School of Chemical and Biological Engineering
Institute of Chemical Processes
Seoul National University
Seoul 08826, Republic of Korea

H. W. Jang
Advanced Institute of Convergence Technology
Seoul National University
Suwon 16229, Republic of Korea

The ORCID identification number(s) for the author(s) of this article can be found under https://doi.org/10.1002/adfm.202400806

DOI: 10.1002/adfm.202400806

material pool is highly restricted owing to its particular requirements, such as high conductivity, electrochemical stability, and more negative band edge positions than those of Ta_3N_5. In addition, the possible phase transformation of Ta_3N_5 during the annealing or post-treatment of HTL for crystallization to obtain electrical conductivity further limits material candidates for HTL. In this respect, previously reported HTLs were dominated by nitrides and oxynitrides formed through one-step thermal nitridation after deposition on the precursor of Ta_3N_5.[16–19]

Conjugated polymers, which have been widely studied in photovoltaic (PV) cells,[28,29] suggest an alternative for the charge transport layer of photoelectrodes. Their delocalized π-electron system along the polymer chain allows for efficient charge transport, maintaining high electrical conductivity.[30] Their structure alternating single and double bonds along the backbone also provides resilience against chemical reactions.[31] Moreover, the diversity of functional groups in the building block not only expands the material candidates but also offers the tunability of band structures for the charge transport layer to be tailored to photoelectrodes. Since these competent characteristics are manifested without annealing or post-treatment after polymerization, the formation of HTL has no effect on the underlying Ta_3N_5 layer. Thus, conformal heterojunction of conjugated polymers with propitious band structures on Ta_3N_5 provides a solution to diminish losses in charge transport of photoanode.

Here, we focus on a new heterojunction of a conjugated polythiophene framework (CPF-TTB) with Ta_3N_5, scrutinizing its hole transport behavior in PEC water oxidation. One-step nitridation forms Ta_3N_5 with a titanium nitride (TiN) bottom electrode surpassing prevalent Ta foil, and their heterostructure with elaborately grown CPF-TTB by electropolymerization is characterized through transmission electron microscopy (TEM). Spectroscopic analyses prove that a decrease in electron density ascribes to the declined electron transport from Ta_3N_5 to CPF-TTB, identifying the formation of conjugated polythiophene. Density functional theory (DFT) calculations theoretically substantiate the efficient charge transport in the heterojunction. The resulting CPF-TTB/Ta_3N_5/TiN photoanode modified with a $NiFeO_x$ cocatalyst yields a remarkable water oxidation photocurrent density of 9.12 mA cm^{-2} at 1.23 V versus a reversible hydrogen electrode (V_{RHE}), which is over 70% of the theoretical value. Systematic studies about charge carrier dynamics authenticate that the accompanied improvement of fill factor emanates from the hole extraction capability of CPF-TTB, which forms type II band alignment with Ta_3N_5. For unbiased solar water splitting, a tandem device consisting of a perovskite/Si PV cell and a PEC cell ($NiFeO_x$/CPF-TTB/Ta_3N_5/TiN photoanode – Pt cathode) acquires a STH conversion efficiency of 6.26%. These results demonstrate an outstanding potential of conjugated polymers as a hole-selective layer, providing insights to design competent metal nitride-based photoelectrode for highly efficient solar water splitting.

2. Results and Discussion

2.1. Structural Characterization of CPF-TTB/Ta_3N_5/TiN

The overall fabrication process of photoanodes was schematically illustrated in **Figure 1a**. To discover the nitride electrode surpassing a Ta foil, which was a conventional electrode material for Ta_3N_5, the Ti, Nb, and Mo thin films were fabricated by e-beam evaporation since their nitrides have a high conductivity in IVb, Vb, and VIb groups, respectively.[32] As a precursor for light absorbers, Ta_2O_5 films were deposited on various metal thin films and Ta foil by e-beam evaporation. One-step nitridation in an ammonia atmosphere made nitrogen substitute oxygen, forming nitride films with different bottom electrodes. The X-ray diffraction (XRD) patterns (Figure S1, Supporting Information) were indexed to the single-phase TiN, NbN, and MoN, showing that highly crystalline nitride phases were well-formed under the high-temperature nitridation. To investigate the optimal bottom electrodes for Ta_3N_5, the photoelectrochemical water oxidation of the fabricated photoanodes was evaluated in a three-electrode cell with 1 M KOH after the $NiFeO_x$ cocatalyst modification. In current density-potential (J–V) curves, the Ta_3N_5 photoanode with TiN electrode exhibited a more cathodic onset potential and higher photocurrent density than that with Ta foil, unlike other metal nitrides. The Ta_3N_5/TiN photoanode also showed the highest half-cell solar-to-hydrogen (HC-STH) conversion efficiency and the most cathodic potential for maximum value among the photoanodes. The thickness of Ti films and nitridation temperature were further adjusted for the optimization of the TiN bottom electrode (Figure S2, Supporting Information). As shown in J–V curves, photoactivity was improved as the nitridation temperature increased, and the optimal thickness of Ti was 80 nm at the highest temperature of 950 °C. We visually checked that the Ta_2O_5/Ti film changed into yellowish TiN and dark-red Ta_3N_5 after nitridation under optimal conditions (Figure S3, Supporting Information). The field-emission scanning electron microscopy (FESEM) images show nanopores were formed on the surface of Ta_3N_5 after thermal nitridation (Figure S4, Supporting Information). In the cross-sectional FE-SEM images, it is observed that Ta_3N_5 and TiN formed an intimate contact that is favorable for electron extraction after nitridation. In Figure 1b, scanning TEM (STEM) image and corresponding energy dispersive X-ray (EDX) mapping also confirm that Ta_3N_5 and TiN formed a well-integrated heterojunction on the sapphire substrate. It is revealed that thickness of TiN increased to around 200 nm after nitridation, indicating diffusion of Ti during nitridation. High-resolution TEM (HRTEM) images clearly denote the highly crystalized Ta_3N_5 and TiN. In Figure 1c, the lattice fringes with interplanar spacings of 3.546 and 2.778 Å correspond to (110) and (023) planes of Ta_3N_5, respectively. The fast Fourier transformation (FFT) patterns present the diffraction spots for (023) and (110) planes, indicating the crystalline orthorhombic Ta_3N_5. The measured interplanar distances of 2.450 Å for both directions of lattice fringes in Figure 1d correspond to (200) and (020) planes of TiN. The FFT showing the diffraction patterns of (020) and (200) planes presents the crystalline cubic TiN.

As a new hole transport layer for Ta_3N_5, a conjugated polythiophene framework was introduced on the Ta_3N_5/TiN photoanode. As a building block, 1,3,5-tris(2-thienyl)benzene (TTB) containing thiophene groups was employed to construct the conjugated polythiophene framework. In various π-conjugated systems, the thiophene-based polymers representatively have high electrical conductivity as well as exceptional chemical and thermal stability.[33,34] The CPF-TTB layer was directly synthesized

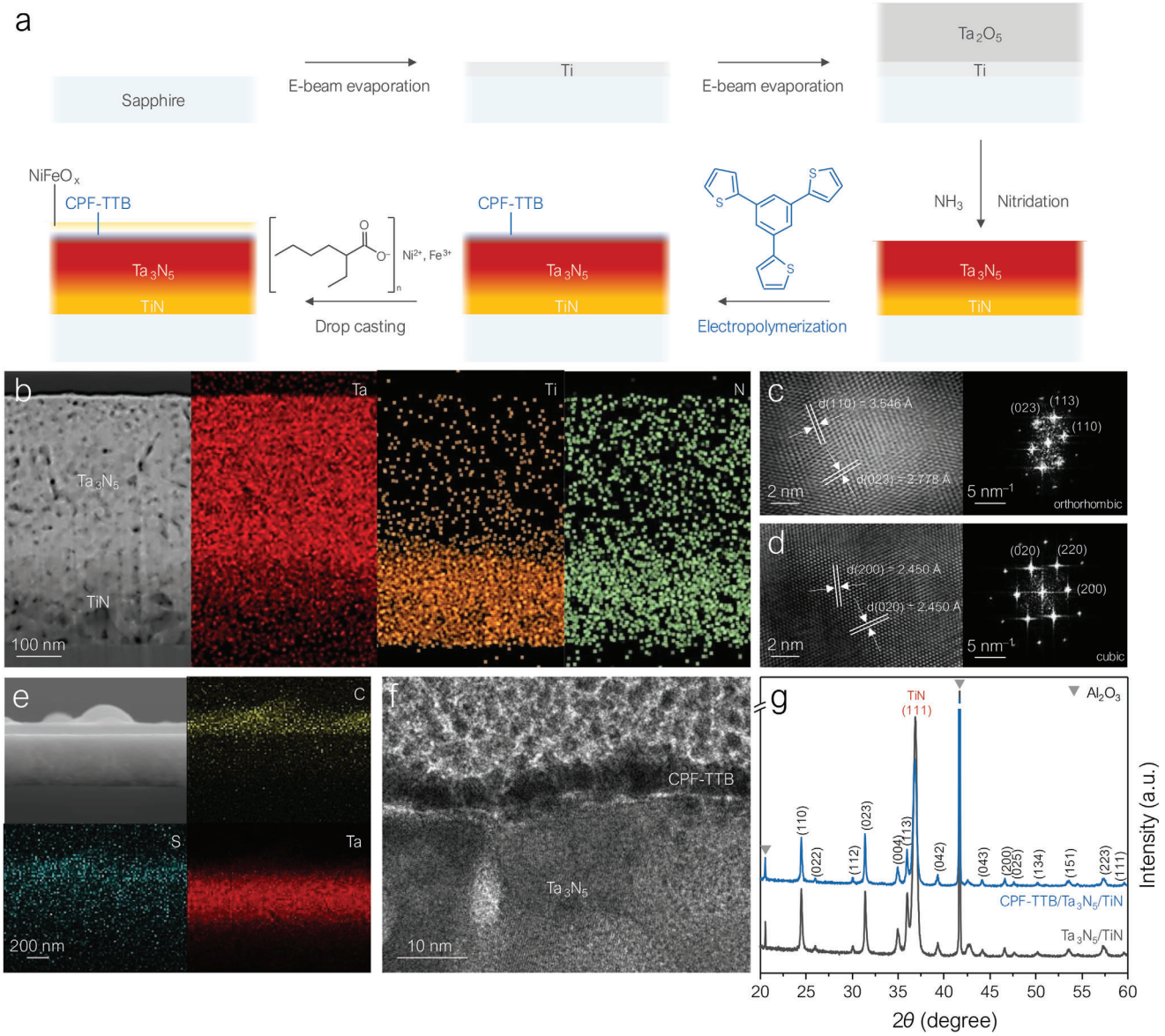

Figure 1. Structural characterization of CPF-TTB/Ta_3N_5/TiN. a) Schematic illustration of the fabrication process for $NiFeO_x$/CPF-TTB/Ta_3N_5/TiN. b) Cross-sectional STEM image and EDX mapping of Ta_3N_5/TiN. HRTEM images and FFT patterns of c) orthorhombic Ta_3N_5 and d) cubic TiN. e) Cross-sectional FESEM image and EDX mapping of CPF-TTB/Ta_3N_5/TiN. f) HRTEM image of CPF-TTB/Ta_3N_5/TiN. g) XRD of Ta_3N_5/TiN and CPF-TTB/Ta_3N_5/TiN.

onto the surface of the Ta_3N_5/TiN through an electropolymerization, which is a simple and cost-effective approach for conjugated polymers.[35] In linear sweep voltammograms of Ta_3N_5/TiN (Figure S5, Supporting Information), current density increases appeared at 0.9 $V_{Ag/AgCl}$ with increasing sweep cycle. As the frameworks grow in polymerization processes, an increment of sites for attaching additional monomers leads to these current density increases.[36] The cross-sectional FESEM image and its EDX mapping in Figure 1e show that the thick CPF-TTB was uniformly covered on the Ta_3N_5. The uniform distribution of C and S elements from CPF-TTB found on the surface of Ta_3N_5 also verified their heterojunction. The C and S elements from top EDX mapping also confirmed the uniform coating of CPF-TTB on Ta_3N_5 (Figure S6, Supporting Information). The thickness of the CPF-TTB was further engineered by reducing the sweep number to maximize light absorption into Ta_3N_5, and the optimized thin layer was characterized using HRTEM. As shown in Figure 1f, the CPF-TTB thin layer with a thickness of around 5 nm was conformally coated on the Ta_3N_5 surface. The amorphous nature of the CPF-TTB was along with the characteristics of electropolymerized polythiophene frameworks in previous works.[37] Lower magnification TEM images (Figure S7, Supporting Information) corroborated that a dense layer was grown without any voids, demonstrating the advantages of electropolymerization in uniformly coating a thin conjugated polymer. The XRD analysis was conducted to characterize the crystal structure of

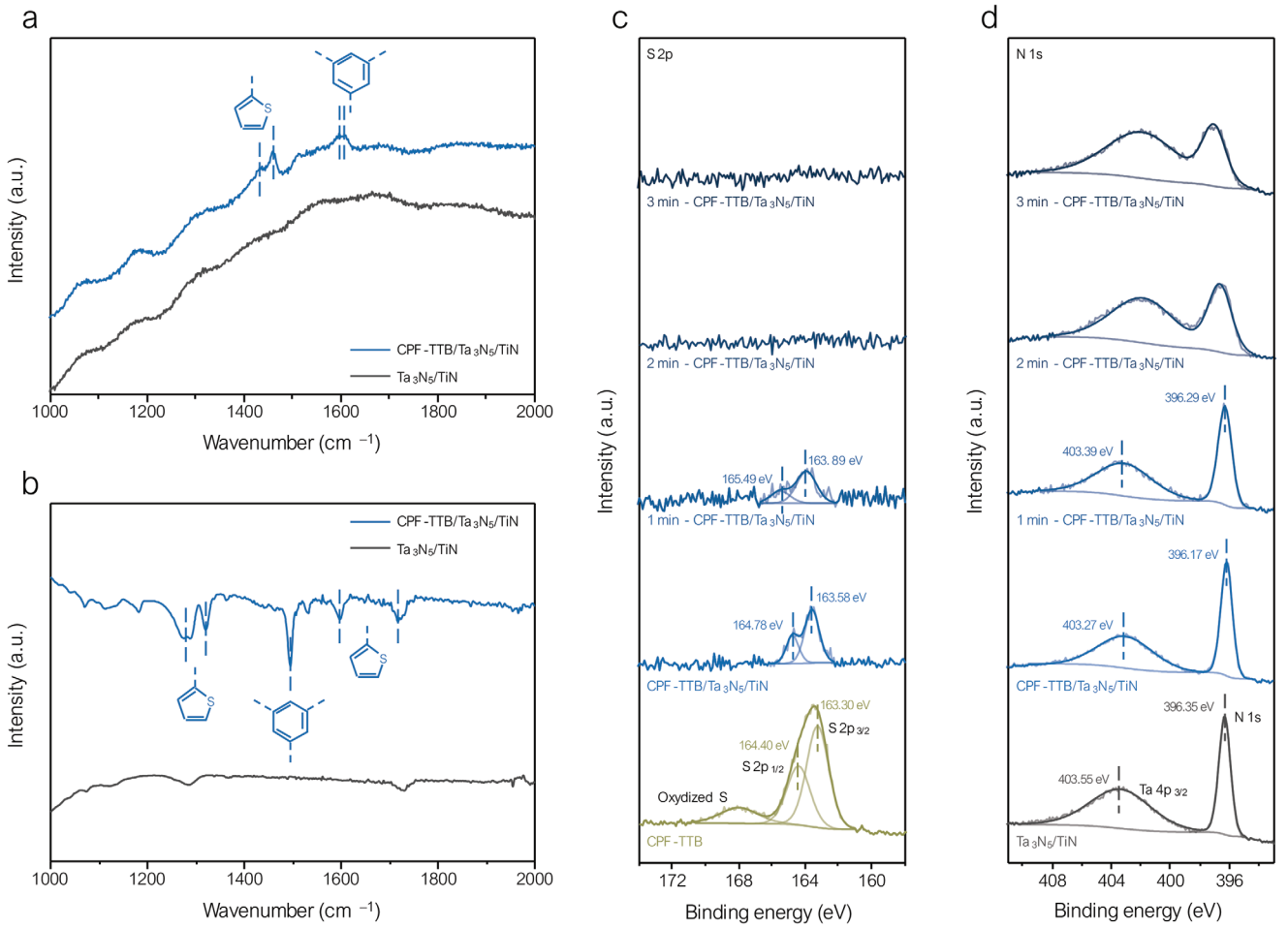

Figure 2. Spectroscopic analysis of CPF-TTB/Ta_3N_5. a) Raman and b) FT-IR spectra of Ta_3N_5/TiN and CPF-TTB/Ta_3N_5/TiN. c) S 2p XPS spectra of CPF-TTB and CPF-TTB/Ta_3N_5/TiN with different Ar plasma (2.5 nm min^{-1}) etching times. d) N 1s XPS spectra of Ta_3N_5/TiN and CPF-TTB/Ta_3N_5/TiN with different Ar plasma (2.61 nm min^{-1}) etching times.

the CPF-TTB/Ta_3N_5/TiN photoanode. As shown in Figure 1g, the diffraction peaks of CPF-TTB/Ta_3N_5/TiN and Ta_3N_5/TiN were indexed to orthorhombic Ta_3N_5 (PDF# 00-019-1291) and cubic TiN (PDF# 01-081-9381), which was consistent with HRTEM analyses in Figure 1c,d. It is also shown that there were no differences in the crystal structures of the photoanode before and after the deposition of CPF-TTB, which corresponds to the amorphous nature of the polythiophene disclosed in Figure 1f.

2.2. Spectroscopic Analysis and DFT Calculations of CPF-TTB/Ta_3N_5

The formation of the CPF-TTB layer was further verified by the chemical vibration in Raman spectroscopy. For Ta_3N_5/TiN, no peaks were identified in the wavenumber range of 1000 to 2000 cm^{-1} in which typical bondings in organic molecules are observed, as shown in **Figure** 2a. In contrast, the characteristic peaks were detected in CPF-TTB/Ta_3N_5/TiN, and the peaks at 1433 and 1459 cm^{-1} were determined to originate from the thiophene functional groups in CPF-TTB. The peaks at 1596 and 1607 cm^{-1} were indexed to the central benzene ring. These peaks were identically found in the Raman spectrum of CPF-TTB formed on FTO (Figure S8, Supporting Information). Fourier transform-infrared (FT-IR) spectra directly revealed the amorphous CPF-TTB layer well-formed on Ta_3N_5/TiN, as exhibited in Figure 2b. The characteristic peaks derived from the thiophene functional groups in CPF-TTB were observed at 1276, 1321, 1596, and 1716 cm^{-1}. Also, the central benzene ring was identified as the sharp peak at 1495 cm^{-1}. The presence of peaks at the same wavenumbers in the FT-IR spectra of CPF-TTB deposited on FTO indicates the successful formation of the CPF-TTB layer (Figure S9, Supporting Information).

X-ray photoelectron spectroscopy (XPS) analysis was conducted to scrutinize the surface chemical and electronic states of Ta_3N_5/TiN, CPF-TTB, and their heterostructure. In survey spectra (Figure S10, Supporting Information), all constituent elements of each sample were detected, and the charge transport investigation was verified by focusing on N 1s, Ta 4f, and S 2p spectra. As shown in Figure 2c, the deconvoluted S $2p_{1/2}$ and S $2p_{3/2}$ peaks in CPF-TTB shifted from 164.40 and 163.30 eV to higher binding energy of 164.78 and 163.58 eV after being deposited

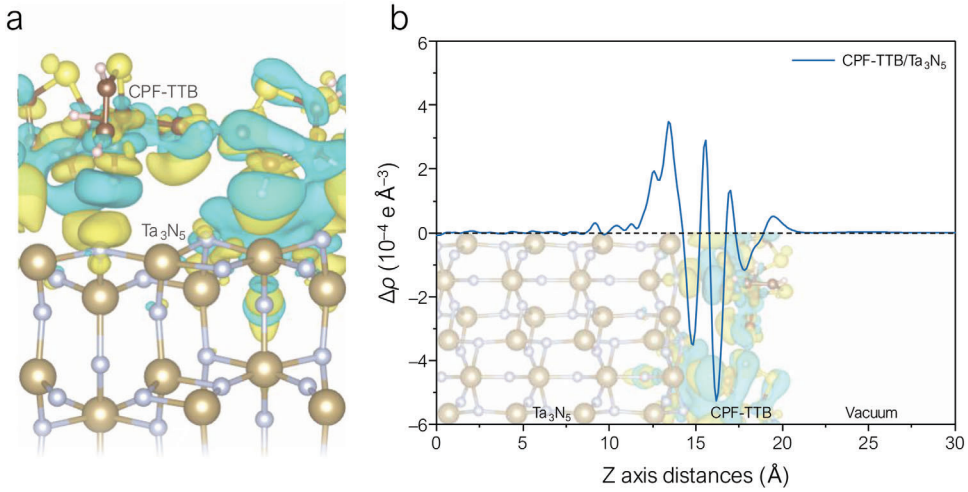

Figure 3. DFT calculations of CPF-TTB/Ta_3N_5. a) Charge density difference across CPF-TTB/Ta_3N_5. b) Planar averaged charge density difference $\Delta\rho$ ($\Delta\rho = \rho_{junction} - \rho_{Ta_3N_5} - \rho_{CPF\text{-}TTB}$) along the *z*-direction for the CPF-TTB/Ta_3N_5.

on Ta_3N_5/TiN. These shifts originated from a reduced electron density of S atoms in the CPF-TTB, implying a declined electron transport from Ta_3N_5 to CPF-TTB.[38] Contrastively, the N 1s peak in Ta_3N_5 shifted from 396.35 eV to a lower binding energy of 396.17 eV by forming a heterojunction of CPF-TTB/Ta_3N_5, as suggested in Figure 2d. Similarly, the deconvoluted Ta $4f_{5/2}$ and $4f_{7/2}$ peaks in Ta_3N_5 also shifted from 26.64 and 24.74 eV to lower binding energies of 26.57 and 24.67 eV in the heterostructure, respectively (Figure S11, Supporting Information). The relative electron transport toward Ta_3N_5 caused these prominent shifts, which were attributed to the enrichment of electron density in Ta_3N_5.[39,40] To further investigate the charge transport behavior, depth profiling was carried out by etching the surface of CPF-TTB/Ta_3N_5/TiN with different Ar plasma irradiation times. The S $2p_{1/2}$ and $S_{3/2}$ peaks gradually decreased over time and completely vanished after 2 min of etching. According to the etching rate of Ar plasma (2.61 nm min^{-1}), the thickness of the CPF-TTB layer is about 5 nm, which is consistent with the HRTEM image in Figure 1f. It is noteworthy that the N 1s peak of 396.14 eV shifts back to a higher binding energy of 396.29 eV after 1 min of etching. As the CPF-TTB layer was etched away, the electron density in Ta_3N_5 was restored to its original state. These spectroscopic analyses prove the formation of the CPF-TTB layer and charge transport in the heterojunction with Ta_3N_5.

The DFT calculations were carried out to identify the spatial distribution of charge density difference, theoretically substantiating the charge transport behavior in the CPF-TTB/Ta_3N_5 heterostructure. To simplify the calculation model, a single-layer CPF-TTB was introduced on the (110) surface of Ta_3N_5 identified in TEM and XRD (Figure S12, Supporting Information). The calculated 3D charge density differences across the CPF-TTB/Ta_3N_5 interfaces are presented in **Figure 3a**. The charge redistribution mainly occurred at the interface of the CPF-TTB/Ta_3N_5, and electron accumulation was observed around the surface of Ta_3N_5. These calculations imply the effective charge transport at the interface of the heterostructure, corresponding to the XPS analysis.[41] Figure 3b shows the planar-averaged charge density difference along the *z*-direction normalized to the CPF-TTB/Ta_3N_5 heterostructure. The calculated charge density difference showing strong electron accumulation on the surface of Ta_3N_5 indicates that electrons primarily transfer from CPF-TTB to Ta_3N_5 through the interface.[42] These results are comparable to spectroscopic analysis and support the crucial role of CPF-TTB in terms of charge transport.

2.3. Photoelectrochemical Water Oxidation

Prior to the photoelectrochemical measurement, a $NiFeO_x$ cocatalyst was introduced to the CPF-TTB/Ta_3N_5/TiN photoanode to further enhance the surface kinetics for water oxidation. Uniform deposition of $NiFeO_x$ from hexane-based precursors by drop-casting enables efficient hole collection from the photoanode.[43] The surface chemical states of the final $NiFeO_x$/CPF-TTB/Ta_3N_5/TiN photoanode were investigated by XPS. The compositional elements of the cocatalyst were detected in Ni 2p and Fe 2p spectra (Figure S13, Supporting Information). The Ni 2p spectrum was deconvoluted into spin-orbit splitting doublets of $2p_{1/2}$ and $2p_{3/2}$ at 873.9 and 856.0 eV. The Fe 2p spectrum was also deconvoluted into the pair of doublets of $2p_{1/2}$ and $2p_{3/2}$ at 725.6 and 712.3 eV. C 1s spectrum was deconvoluted into three peaks at 288.3, 285.4, and 284.5 eV, corresponding to C═O, C—O, and C—C bondings, respectively, which were derived from the 2-ethylhexanoate in Ni-Fe precursor.

The photoelectrochemical water oxidation performance of the fabricated photoanodes was measured in 1 M KOH (pH 14) using a three-electrode cell under AM1.5G illumination. The PEC characteristics were examined with a focus on comparing Ta_3N_5/TiN and CPF-TTB/Ta_3N_5/TiN with and without the $NiFeO_x$ cocatalyst. As shown in **Figure 4a**, the CPF-TTB/Ta_3N_5/TiN photoanode exhibited an increased photocurrent density of 1.52 mA cm^{-2} at 1.23 V_{RHE}, which is ≈2.6 times improvement compared to the Ta_3N_5/TiN photoanode (0.58 mA cm^{-2}). The cathodic shift of onset potential was also identified after the modification of CPF-TTB in *J*–*V* curves under non-chopped light (Figure S14, Supporting Information). The loading of the

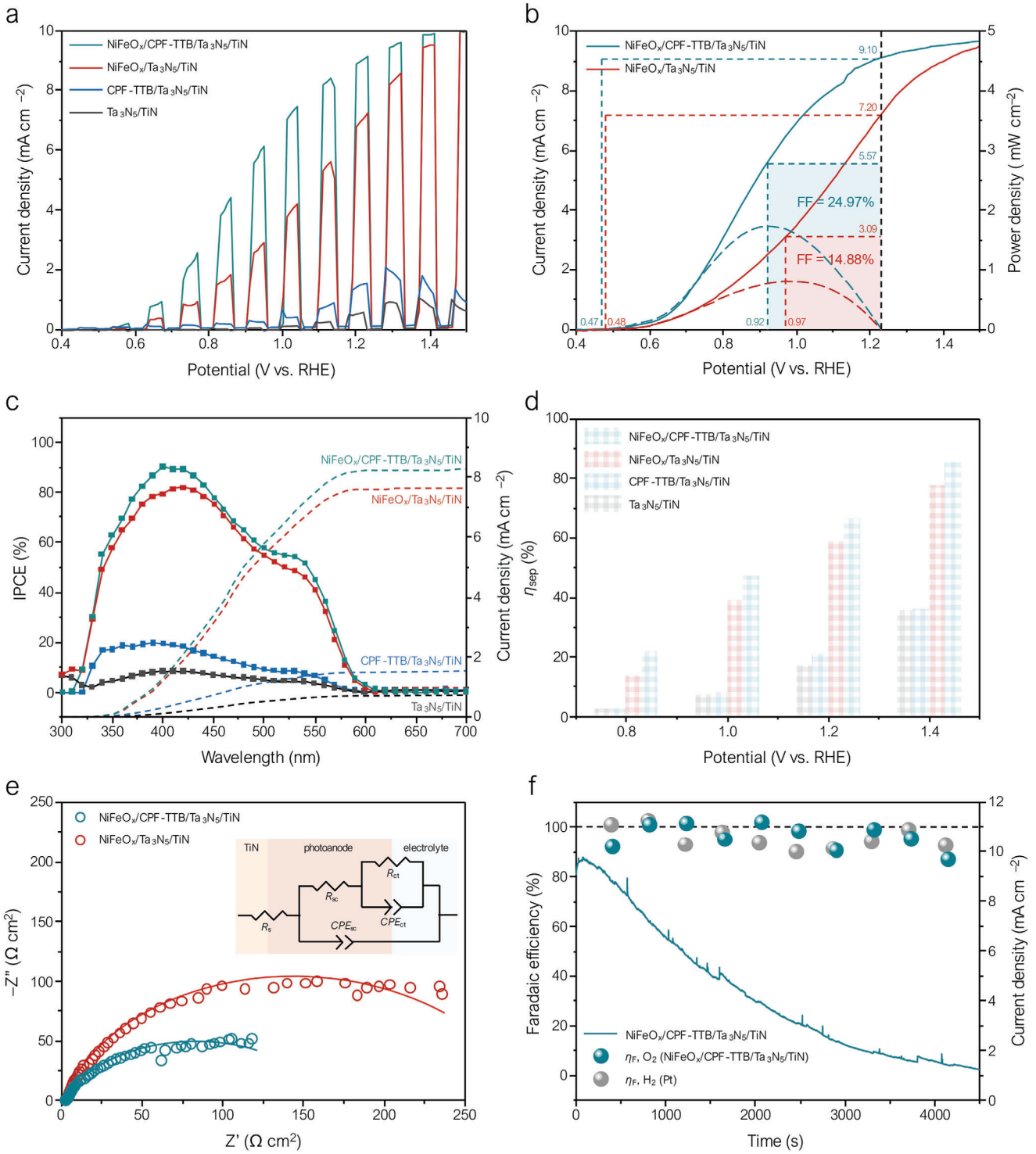

Figure 4. Photoelectrochemical water oxidation. a) *J–V* curves of Ta_3N_5/TiN, CPF-TTB/Ta_3N_5/TiN, $NiFeO_x$/Ta_3N_5/TiN, and $NiFeO_x$/CPF-TTB/Ta_3N_5/TiN photoanodes. b) Fill factors of $NiFeO_x$/Ta_3N_5/TiN and $NiFeO_x$/CPF-TTB/Ta_3N_5/TiN photoanodes. c) IPCE spectra at 1.23 V_{RHE}, integrated current densities, and d) charge separation efficiencies of Ta_3N_5/TiN, CPF-TTB/Ta_3N_5/TiN, $NiFeO_x$/Ta_3N_5/TiN, and $NiFeO_x$/CPF-TTB/Ta_3N_5/TiN photoanodes. e) EIS Nyquist plots at 1.23 V_{RHE} of $NiFeO_x$/Ta_3N_5/TiN and $NiFeO_x$/CPF-TTB/Ta_3N_5/TiN photoanodes. f) Faradaic efficiency and *J-t* curve at 1.23 V_{RHE} of $NiFeO_x$/CPF-TTB/Ta_3N_5/TiN photoanode. All measurements were conducted in 1 M KOH (pH 14) under AM1.5G 1 sun illumination.

cocatalyst led to a more conspicuous enhancement. The $NiFeO_x$/CPF-TTB/Ta_3N_5/TiN photoanode showed a noticeable photocurrent density of 9.12 mA cm^{-2} at 1.23 V_{RHE}, which is a marked enhancement compared to the $NiFeO_x$/Ta_3N_5/TiN photoanode (7.25 mA cm^{-2}). Another notable characteristic is that the introduction of CPF-TTB made the larger polarization compared to pristine Ta_3N_5/TiN after loading the cocatalyst. This feature was plainly revealed in the fill factor, as exhibited in Figure 4b. The FF is calculated as the ratio of rectangularity between the entire *J–V* curve and the maximum power point of HC-STH. The lower potential of $NiFeO_x$/CPF-TTB/Ta_3N_5/TiN for the maximum power point (0.92 V_{RHE}) compared to that of $NiFeO_x$/Ta_3N_5/TiN (0.97 V_{RHE}) denotes that CPF-TTB contributed to a high-power photoanode. When the CPF-TTB was introduced between $NiFeO_x$ and Ta_3N_5, the FF increased from 14.88 to 24.97%. The significant enhancement of the fill factor was ascribed to the reduction of voltage loss as well as the increase in current density, signifying that CPF-TTB effectively facilitated hole transport from Ta_3N_5 to $NiFeO_x$. In Figure 4c, the incident-photon-to-current conversion efficiency (IPCE) at 1.23 V_{RHE} was provided to evaluate the overall photoactivity of four types of photoanodes. All photoanodes based on Ta_3N_5 with a band gap of 2.1 eV as a light absorber obtained IPCE values up to 600 nm. Similar to the tendency in the *J–V* curves, the photoanodes with CPF-TTB achieved a higher IPCE than those without the layer, irrespective of the presence of $NiFeO_x$ cocatalyst. To reverify the photocurrent density, the product of IPCE spectra and photon flux was integrated over the wavelength. The integrated current densities of all photoanodes were consistent with the current densities at 1.23 V_{RHE} in Figure 4a.

To expose the effect of CPF-TTB, the charge separation efficiency (η_{sep}) was calculated using *J–V* curves with 0.2 M Na_2SO_3 as a hole scavenger (Figure S15, Supporting Information). As displayed in Figure 4d, the η_{sep} value of CPF-TTB/Ta_3N_5/TiN was slightly higher than that of Ta_3N_5/TiN. However, with the $NiFeO_x$ cocatalyst, the increases in η_{sep} value were more pronounced across the entire potential range, indicating the effective hole transport of CPF-TTB between Ta_3N_5 and $NiFeO_x$. As shown in Figure 4e, the electrochemical impedance spectroscopy (EIS) was carried out at 1.23 V_{RHE} to corroborate the hole transport ability of CPF-TTB, and Nyquist plots were fitted with an equivalent circuit consisting of series resistance (R_s) and the charge transfer resistances in the semiconductor (R_{sc}) and photoanode/electrolyte interface (R_{ct}). As tabulated in Table S1 (Supporting Information), the fitted R_{ct} of $NiFeO_x$/CPF-TTB/Ta_3N_5/TiN (161.6 Ω cm^2) is lower than that of $NiFeO_x$/Ta_3N_5/TiN (285.0 Ω cm^2), implying a more efficient interfacial charge transfer. These trends of $NiFeO_x$/CPF-TTB/Ta_3N_5 having a smaller semicircle were also observed in EIS measured at 0.6 V_{RHE} near the onset potential (Figure S16, Supporting Information). The introduction of CPF-TTB diminished the charge transfer resistance, resulting in improved PEC performance. The durability of photoanodes for water oxidation was evaluated by the *J-t* curves at 1.23 V_{RHE} (Figure S17, Supporting Information). In line with previous reports,[44,45] the severe photo-corrosive nature of Ta_3N_5 caused a rapid current drop in the Ta_3N_5/TiN photoanode. However, CPF-TTB protected the surface of Ta_3N_5 from the photocorrosion, and the CPF-TTB/Ta_3N_5/TiN photoanode showed a more delayed drop in current density. In addition, after the modification of the cocatalyst, the $NiFeO_x$/CPF-TTB/Ta_3N_5/TiN photoanode showed a more delayed drop in current density compared to the $NiFeO_x$/Ta_3N_5/TiN photoanode. Faradaic efficiency was evaluated by the gas chromatography of the evolved gas from the $NiFeO_x$/CPF-TTB/Ta_3N_5/TiN photoanode and Pt cathode. As shown in Figure 4f, Faradaic efficiencies of approaching 100% in both photoanode and cathode demonstrate that generated charges are fully consumed by the water splitting into oxygen and hydrogen. Although the photoanode in which both the CPF-TTB layer and $NiFeO_x$ cocatalyst were modified showed the most stable operation, the current decay in long-term chronoamperometry indicates that they are still insufficient as a protective layer. The characterization after the stability test shows a decrease in PEC performance and changes in the surface morphology of Ta_3N_5 (Figure S18, Supporting Information). The exposure of nanopores of Ta_3N_5 after the stability test shows that $NiFeO_x$ and CPF-TTB did not completely protect the surface of Ta_3N_5, indicating that continual studies are required to further prevent the photocorrosion of Ta_3N_5.

2.4. Charge Carrier Dynamics

Mott-Schottky (M-S) analysis was employed to identify the change in surface energetics of the photoanodes according to the CPF-TTB layer. As shown in **Figure 5a**, the flat-band potential of the Ta_3N_5/TiN photoanode is at 0.02 V_{RHE}, and the slope of the M-S plot changes at the high potential region over 0.36 V_{RHE}. At low potential, the surface states of Ta_3N_5 induce the Fermi level pinning, which weakens band bending and makes the difference in slope depending on the potential region.[46] The density of surface states decreases at the high potential, causing larger band bending and increasing the slope of the M-S plot. The CPF-TTB/Ta_3N_5/TiN photoanode had a similar flat band potential of 0.00 V_{RHE} compared to the Ta_3N_5/TiN photoanode. However, the slope transition occurred at a lower potential of 0.27 V_{RHE}, which means it requires a lower potential to overcome the Fermi level pinning. That is, CPF-TTB stabilized the surface of Ta_3N_5 by reducing the density of surface states. The carrier concentration was calculated by the slope at a low potential region based on the following equation:

$$C^{-2} = \left(2/\varepsilon\varepsilon_0 A^2 e N_D\right)\left[V - E_{FB} - \left(k_B T\right)/e\right] \quad (1)$$

where C is the capacitance of the space charge layer (F), ϵ is dielectric constant (~110), ϵ_0 is the permittivity of vacuum (8.854 × 10^{-12} F m^{-1}), A is the surface area (m^2), e is the electron charge (1.062 × 10^{-19} C), V is the applied potential (V), E_{FB} is the flat band potential (V), k_B is the Boltzmann constant (1.381 × 10^{-23} F m^{-1}), and T is the temperature (298 K). As tabulated in Table S2 (Supporting Information), CPF-TTB/Ta_3N_5/TiN have a higher carrier concentration of 9.326 × 10^{18} cm^{-3} compared to that of Ta_3N_5/TiN (5.064 × 10^{18} cm^{-3}), suggesting that CPF-TTB improved charge separation.

The open-circuit potential (OCP) transient decay profile was utilized to further investigate the charge carrier dynamics of the photoanodes.[47–49] The normalized OCP profiles exhibited that the CPF-TTB/Ta_3N_5/TiN had faster decay than Ta_3N_5/TiN (Figure S19, Supporting Information). The heterojunction effectively enabling charge separation under illumination results in

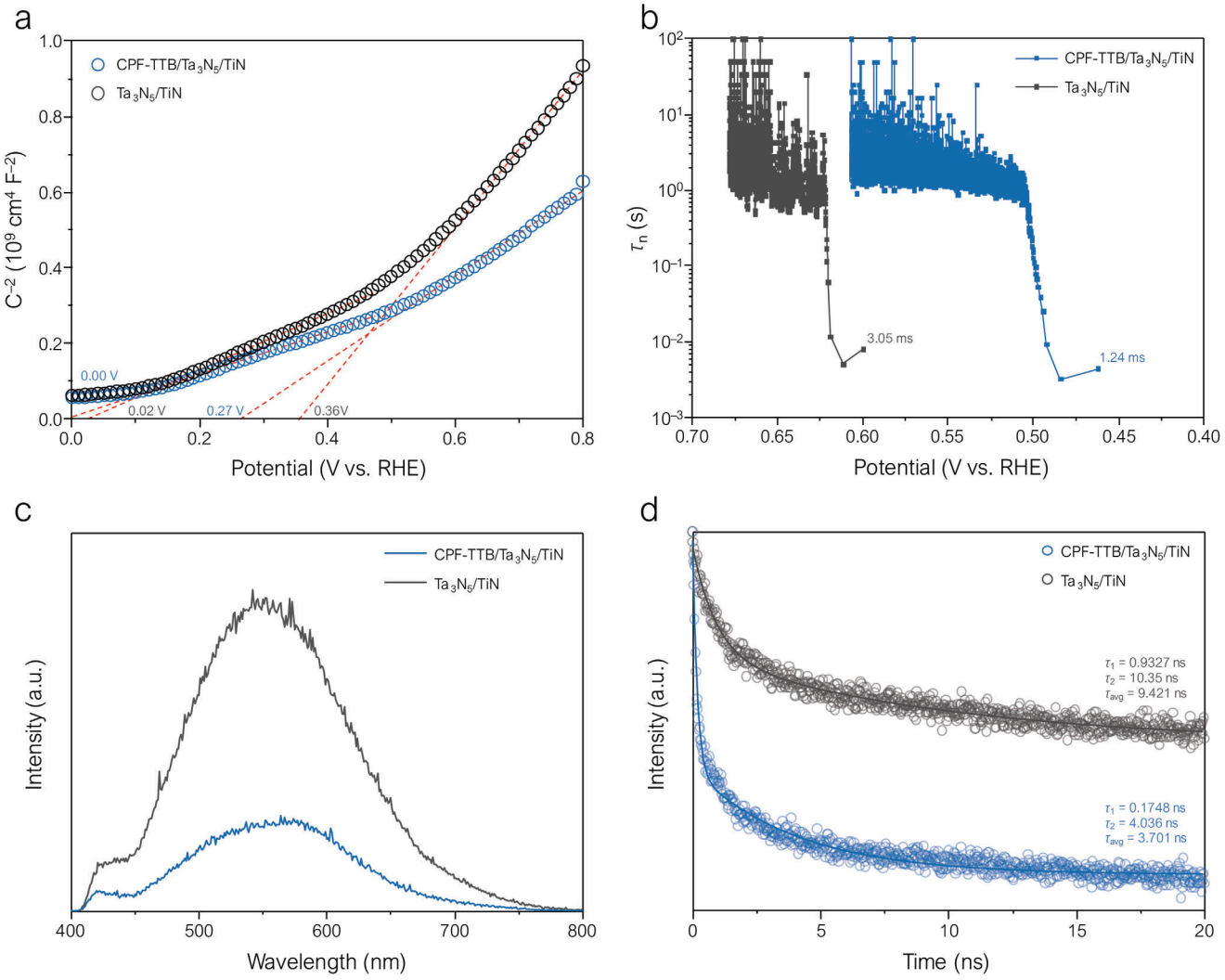

Figure 5. Charge carrier dynamics. a) M-S plots and b) OCP-derived carrier lifetimes of Ta_3N_5/TiN and CPF-TTB/Ta_3N_5/TiN. c) Steady-state and d) time-resolved PL of Ta_3N_5/TiN and CPF-TTB/Ta_3N_5/TiN.

a significant charge accumulation within the depletion region. Thus, when the illumination is stopped, the enhanced charge recombination causes a fast decay. In other words, the faster decay profile indicates the larger charge recombination in light-off, conversely implying that the heterojunction expedites charge separation under illumination. The carrier lifetime (τ_n) was quantified as a function of OCP by the following equation:

$$\tau_n = -\left[\left(k_B T\right)/e\right]\left(d\mathrm{OCP}/dt\right)^{-1} \quad (2)$$

where dOCP/dt is the time derivative of the OCP transient decay. As exhibited in Figure 5b, CPF-TTB/Ta_3N_5/TiN has a carrier lifetime of 1.24 ms, which is shorter than that of Ta_3N_5/TiN (3.05 ms). The short carrier lifetime derived by the faster carrier relaxation after light-off implies that photogenerated carriers are efficiently transported to CPF-TTB under illumination.[50,51] The expedited decay kinetics of CPF-TTB/Ta_3N_5/TiN also corroborate the reduced charge recombination in the depletion region and the hole transport capability of CPF-TTB.

To further reveal the charge separation behavior of Ta_3N_5 with and without the CPF-TTB layer, the photoluminescence (PL) analysis was conducted. The steady-state PL spectra in Figure 5c display peaks at 560 nm, which are derived from radiative charge recombination due to the defect states within Ta_3N_5.[52] The PL intensity was quenched when Ta_3N_5 film was coated with CPF-TTB, presenting it successfully suppressing the radiative charge recombination.[53] This ability to extract photocarriers is consistent with the result of reduced OCP-derived lifetime and enhanced charge separation efficiency. The charge recombination behavior was further clarified by time-resolved PL (TRPL) measured at PL peak wavelength of 560 nm. The TRPL decay curves in Figure 5d were fitted with the following biexponential decay function consisting of two carrier lifetimes (τ_1 and τ_2):

$$I(t) = A_1 e^{-t/\tau_1} + A_2 e^{-t/\tau_2} \quad (3)$$

where I and A are intensity and amplitude, respectively. The τ_1 values, which is the initial fast decay component associated with

electron trapping,[54] are not significantly different (0.1748 and 0.9327 ns), as listed in Table S3 (Supporting Information). In contrast, there was a pronounced difference in the τ_2 values, which is the ensuing slow decay component related to radiative interband recombination.[55] The smaller τ_2 value for CPF-TTB/Ta_3N_5/TiN (4.036 ns) than that of Ta_3N_5/TiN (10.35 ns) is indicative of the more efficient photogenerated hole extraction through the CPF-TTB layer. The average carrier lifetime (τ_{avg}) of CPF-TTB/Ta_3N_5/TiN (3.701 ns) is also shorter than that of Ta_3N_5/TiN (9.421 ns), synthetically proving the hole extraction ability of CPF-TTB. These observations about charge carrier dynamics support that the introduction of CPF-TTB contributed to comprehensively improving the PEC performances.

2.5. Band Structures and Unbiased Solar Water Splitting

To elucidate the band structure of the heterojunction, the band edge positions of TiN, Ta_3N_5, and CPF-TTB were analyzed by ultraviolet photoelectron spectroscopy (UPS). The secondary electron emission (SEE) spectra revealed the Fermi levels of Ta_3N_5 (4.26 eV) and CPF-TTB (4.09 eV) as well as various bottom electrodes containing TiN (4.63 eV) by subtracting the cut-off energy from the He I excitation energy of 21.22 eV (Figure S20, Supporting Information). The valence band (VB) spectra at the low binding energy region disclosed that the valence band edges of Ta_3N_5 and CPF-TTB are positioned 1.69 and 1.91 eV below respective Fermi levels. The ultraviolet-visible (UV-vis) spectroscopy was employed to measure the optical band gap and specify conduction band edges. The Tauc plots calculated by UV-vis transmittance and reflectance revealed the optical band gap of Ta_3N_5 (2.13 eV) and CPF-TTB (2.66 eV) (Figure S21, Supporting Information). Combining UPS and UV-vis spectra, energy band diagrams of TiN, Ta_3N_5, and CPF-TTB were experimentally determined, as shown in **Figure 6a**. In the band structure of CPF-TTB/Ta_3N_5/TiN, the TiN bottom electrode is advantageous for the efficient extraction of photoexcited electrons from Ta_3N_5. Moreover, the CPF-TTB and Ta_3N_5 construct a type II heterojunction, where it is energetically favorable to not only extract photogenerated holes but also block electron transport to the electrolyte. As a hole-selective layer, CPF-TTB boosts overall PEC water oxidation performances by restraining charge recombination and expediting hole transport from Ta_3N_5 to $NiFeO_x$, as illustrated in Figure 6a.

Unbiased solar water splitting was accomplished by fabricating a tandem device combining the $NiFeO_x$/CPF-TTB/Ta_3N_5/TiN photoanode with a photovoltaic cell. For high STH conversion efficiency, an operating point of the tandem device should be formed at the high-voltage region where the photoanode produces high current density.[56,57] Thus, to supply sufficient photovoltage, we introduced a halide perovskite/Si solar cell, which generated a high open-circuit voltage of 1.89 V with a short-circuit current density of 20.24 mA cm^{-2} (Figure S22, Supporting Information). The tandem device was measured under parallel illumination mode (mode P), where the light was independently irradiated into both light absorbers,[58] due to the opaque characteristic of the Ta_3N_5 photoanode. The 2-electrode *J-V* curves of the PV and PEC cell comprising a Pt cathode and the $NiFeO_x$/CPF-TTB/Ta_3N_5/TiN photoanode were recorded under mode P, as shown in Figure 6b. The operating current density (J_{OP}) determined by the intersection of 2-electrode *J-V* curves of the PV and PEC cell was 10.18 mA cm^{-2} at 1.71 V, which corresponded to a STH conversion efficiency of 6.26%. The chronoamperometry of the PV-PEC tandem device without external bias was conducted in KOH under mode P. The *J-t* curve in Figure 6c shows that the initial current density is well-matched with the J_{OP} and corresponding STH conversion efficiency, but it decreases significantly with time, which is related to fast photocorrosion of Ta_3N_5 in the high-voltage region. These results show that the practical application of the tandem device is still insufficient, implying that continuous studies are necessary to further stabilize the surface of Ta_3N_5 for unbiased solar water splitting.

3. Conclusion

In summary, we designed a new heterojunction of CPF-TTB/Ta_3N_5/TiN focused on effective charge transport, assessing its PEC water oxidation activity with modification of $NiFeO_x$ cocatalyst. Raman and FT-IR spectra confirmed the electropolymerized CPF-TTB layer on Ta_3N_5, and their conformal heterojunction was confirmed with HRTEM. The XPS analysis and its depth profiling elucidated the charge separation behavior inhibiting electron transport from Ta_3N_5 to CPF-TTB. The planar-averaged charge density difference by the DFT calculations further corroborated efficient charge transport between CPF-TTB and Ta_3N_5. After loading a cocatalyst, the $NiFeO_x$/CPF-TTB/Ta_3N_5/TiN photoanode generated an outstanding water oxidation photocurrent density of 9.12 mA cm^{-2} at 1.23 V_{RHE}, which is not only over 70% of the theoretical current density but also noticeable value among previous works (Table S4, Supporting Information). Also, the enhanced fill factor after deposition of CPF-TTB stemmed from expedited hole transport, which was disclosed by the suppressed charge recombination and increased charge density in the investigation of charge carrier dynamics. It was revealed that CPF-TTB forms a type II band alignment with Ta_3N_5 and boosts PEC water oxidation performances by efficient charge transport as a hole-selective layer. The PV-PEC tandem device combined with the perovskite/Si solar cell attained an unbiased solar water splitting with a STH conversion efficiency of 6.26%. This work demonstrated for the first time the charge transport behavior of conjugated polythiophene on Ta_3N_5, expanding the development strategy of the Ta_3N_5 photoanode. Our approach provides a novel perspective in the design of high-efficiency organic–inorganic hybrid photoelectrode for solar water splitting.

4. Experimental Section

Fabrication of Ta_3N_5/TiN Photoanodes: The *c*-plane sapphire wafer (Hi-Solar, single-side polished, 430 ± 25 µm thick) and Ta foil (Alfa Aesar, 99.95%, 0.25 mm thick) were diced into 1 × 1 cm^2 size. The pieces of sapphire substrate and Ta foil were washed in an ultrasonic bath with acetone, isopropanol, and deionized water for 20 min, followed by drying with N_2 flow. The Ti films were deposited on the sapphire substrates by the e-beam evaporation of Ti pellets (iTASCO, 99.99%). The films varying the thickness from 40 to 200 nm were deposited with a rate of 0.5 Å s^{-1} and pressure of 2.0 × 10^{-6} Torr. For comparison, Nb and Mo films were also formed on the sapphire substrates by e-beam evaporation of Nb (iTASCO, 99.9%) and Mo pellets (iTASCO, 99.95%) under the same conditions. The

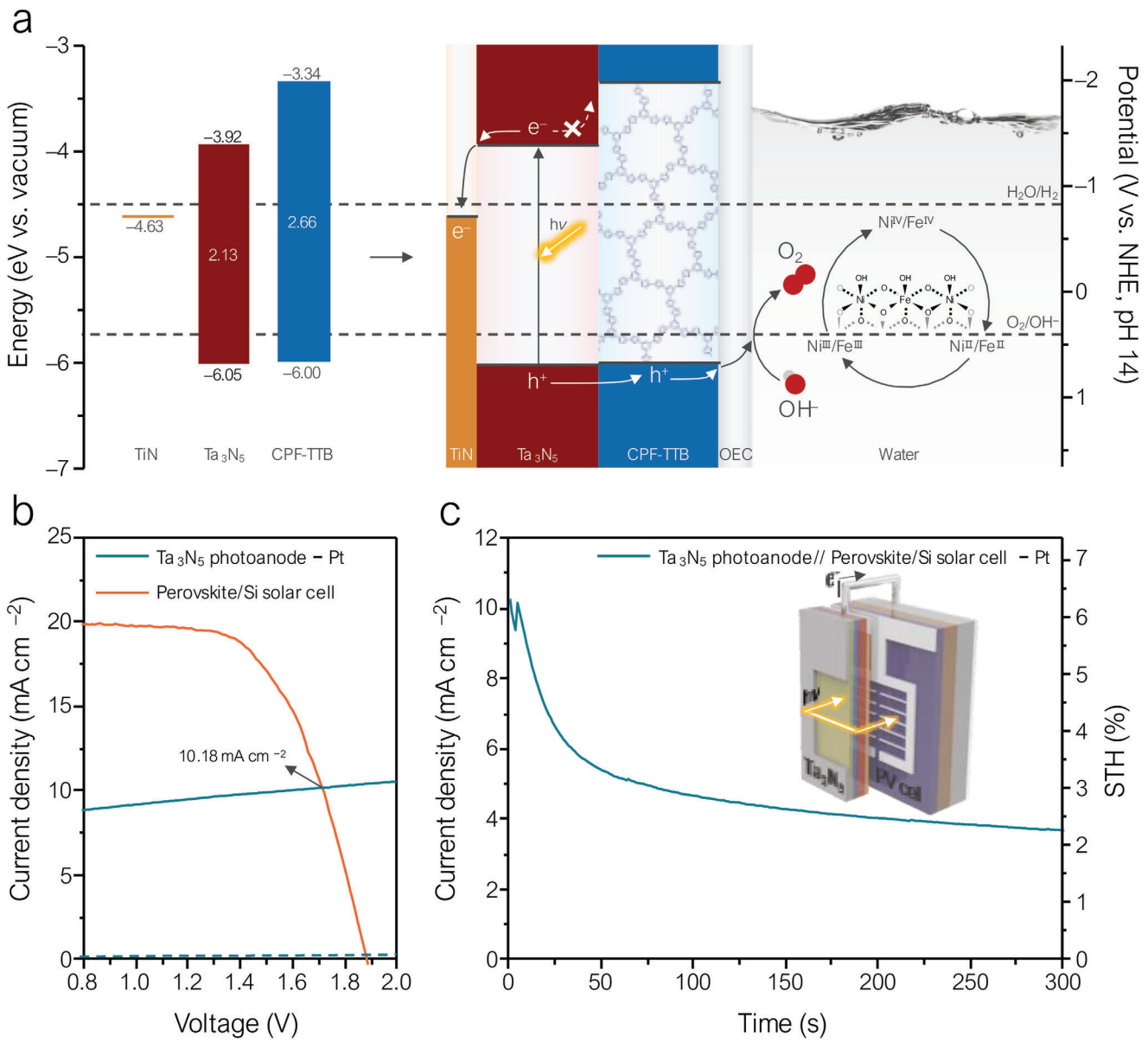

Figure 6. Band structures and unbiased solar water splitting. a) Experimentally determined energy band diagrams of TiN, Ta_3N_5, and CPF-TTB and schematic illustration of the $NiFeO_x$/CPF-TTB/Ta_3N_5/TiN photoanode during PEC water oxidation. b) 2-electrode *J-V* curves of $NiFeO_x$/CPF-TTB/Ta_3N_5/TiN photoanode – Pt cathode and perovskite/Si solar cell (dashed line: *J-V* curve under light-off). c) *J-t* curves of the PV-PEC tandem device under mode P. All measurements were conducted in 1 M KOH (pH 14) under AM1.5G 1 sun illumination.

480 nm-thick Ta_2O_5 films were deposited on Ti, Nb, Mo films, and Ta foils by the e-beam evaporation of Ta_2O_5 granules (iTASCO, 99.99%) with a rate of 1.0 Å s^{-1} and pressure of 2.0×10^{-5} Torr. Prior to the one-step thermal nitridation, the quartz tube furnace containing the as-deposited films was purged by the N_2 flow of 50 sccm for 60 min. Under the NH_3 (99.999%) flow of 250 sccm, the as-deposited Ta_2O_5/Ti films were nitridated into Ta_3N_5/TiN films at a temperature of 950 °C for 150 min with a ramping rate of 5 °C min^{-1}.

Synthesis of CPF-TTB Hole Transport Layers: The CPF-TTB films were synthesized by electropolymerization on Ta_3N_5/TiN photoanodes. A 0.1 M tetrabutylammonium perchlorate (TCI, 98%) was dissolved in 76 mL of the mixed solvent (dichloromethane (Daejung, 99.5%):acetonitrile (Daejung, 99.7%) = 1:3, in v/v) to obtain a conductivity. The 4 mM 1,3,5-tris(2-thienyl)benzene (TCI, 98%) was dissolved in the solution for 10 min. The Ta_3N_5/TiN photoanode was chemically etched with a mixed etchant (HF (Alfa Aesar, 49%):HNO_3 (Junsei, 60%):H_2O = 1:2:7, in v/v) for 20 s and consisted of the three-electrode cell with Ag/AgCl and Pt plate. The potential was linearly swept seven times in the range of 0 to 1.3 $V_{Ag/AgCl}$ at a scan rate of 20 mV s^{-1}. After electropolymerization, the photoanodes were rinsed with acetonitrile and ethanol, followed by drying with N_2 flow.

Synthesis of $NiFeO_x$ Cocatalysts: The $NiFeO_x$ cocatalysts were coated by the drop-casting modified from the previous method.[59] The precursor solution with a total concentration of 50 mM metal complex was prepared by dissolving nickel (II) 2-ethylhexanoate (Sigma-Aldrich, 78% w/w in 2-ethylhexanoic acid) and iron(III) 2-ethylhexanoate (Alfa Aesar, 50% w/w in mineral spirits) in *n*-hexane (Acros, 99%). The photoanodes were heated

at 140 °C for 45 min in the air after the 20 µL of precursor solution was dripped on their surface.

Fabrication of the Perovskite/Si Solar Cells: The perovskite/Si solar cells were fabricated using the previous method.[60] A 20 nm and 80 nm-thick indium tin oxide (ITO) layers were deposited with radio frequency sputtering on the top and bottom of the Si cell, respectively. A 7 mg mL^{-1} poly(triarylamine) (Sigma-Aldrich) solution in toluene was spin-coated at 6000 rpm for 30 s and annealed at 100 °C for 10 min. For a perovskite solution, 1.3 M $Cs_{0.3}DMA_{0.2}MA_{0.5}PbI_3$ with 10 mol% MACl (Lumtec, 99.5%), 1.5 mol% PEASCN (Greatcell Solar), and 2 mol% $Pb(SCN)_2$ additives was dissolved in the mixed solvent (*N*-methyl-2-pyrroldone (Sigma-Aldrich, 99%):dimethylformamide (Sigma-Aldrich, 99.8%) = 1:4, in v/v). The solution was spin-coated at 3000 rpm for 24 s, and 50 µL of methyl acetate (Sigma-Aldrich, 99%) was dripped during the spinning. After annealing at 100 °C for 10 min, a 15 nm-thick C_{60} (Nano-C) layer was deposited by thermal evaporation, and 0.2 wt.% polyethyleneimine (Sigma-Aldrich, 80% ethoxylated) solution in methanol was spin-coated at 6000 rpm for 30 s. A 40 nm-thick ITO layer was deposited by radio frequency sputtering, and a 500 nm-thick Ag grid was deposited by thermal evaporation. A MgF_2 (Sigma-Aldrich, 99.99%) anti-reflection layer was finally deposited to a thickness of 105 nm.

Characterizations: The crystal structures of the samples were determined by XRD (D8 Advance, Bruker) with Cu *Kα* (1.5406 Å) radiation. The surface structures and EDX mapping of the films were characterized by FESEM (MERLIN Compact, ZEISS). A TEM (JEM-2100F, JEOL) was utilized to obtain STEM images, EDX mapping, HRTEM images, and FFT patterns of Ta_3N_5/TiN and CPF-TTB/Ta_3N_5/TiN. The specimen for TEM was prepared by a focused ion beam (Helios G4, Thermo Fisher). Raman spectra were obtained using a Raman spectrometer (LabRAM HR Evolution, HORIBA) with a 532 nm excitation laser. FT-IR spectra were measured with transmittances of a FT-IR spectrometer (Nicolet iS50, Thermo Fisher). The chemical states were analyzed by XPS (Versaprobe III, ULVAC-PHI) with monochromatic Al *Kα* (1486.6 eV) radiation. Depth profiling was performed by adjusting the etching time of Ar plasma (1 kV) with a rate of 2.61 nm min^{-1}, and the spectra were fitted using CasaXPS software (CasaXPS). PL spectra were recorded by a fluorescence spectrometer (FlouTime 300, PicoQuant) with a 405 nm excitation laser. The TRPL data measured at a wavelength of 560 nm was fitted with FlouFit software (PicoQuant). Band structures were analyzed by the UPS (AXIS Nova, KRATOS) with He I (21.22 eV) source. An UV-vis spectrometer (V-770, JASCO) was used to acquire the transmittance and reflectance spectra for Tauc plots of Ta_3N_5 and CPF-TTB.

Photoelectrochemical Measurements: All measurements were conducted with a potentiostat (nStat, Ivium Technologies) on a three-electrode cell consisting of the Ag/AgCl electrode and Pt mesh in 1 M KOH (pH 14). The potential was converted into RHE by the Nernst equation:

$$E_{RHE} = E_{Ag/AgCl} + E^0{}_{Ag/AgCl} + 0.059 \times pH \quad (4)$$

where $E_{Ag/AgCl}$ is the measured potential (V) versus the Ag/AgCl electrode, and $E^0{}_{Ag/AgCl}$ is a standard potential (0.198 V) of the Ag/AgCl electrode. For PEC measurements, a Xe arc lamp (LS 150, Abet Technologies) was used as a light source, where the illumination and intensity were calibrated with an AM1.5G filter and Si photodiode (S300, McScience), respectively. The potential in *J-V* curves was swept toward the anodic direction with a scan rate of 20 mV s^{-1} under chopped illumination. The HC-STH conversion efficiency was calculated by *J–V* curves using the following equation:

$$HC-ST\ (\%) = J_{ph} \times \left(1.23 - V_{app}\right) / P_{in} \quad (5)$$

where J_{ph} is the photocurrent density (mA cm^{-2}), V_{app} is the applied potential (V) versus RHE, and P_{in} is the irradiance (100 mW cm^{-2}) of the simulated sunlight. The FF was calculated by *J–V* curves using the following equation:

$$FF\ (\%) = [J_{MP} \times (1.23 - V_{MP})] / [J_{SC} \times (1.23 - V_{ON})] \quad (6)$$

where the J_{MP} and V_{MP} are the current density and potential at the maximum power point, J_{SC} is the current density at 1.23 V_{RHE}, and V_{ON} is the onset potential. The IPCE at 1.23 V_{RHE} was recorded as the wavelength controlled by a monochromator (MonoRa150i, Dongwoo Optron). The spectral current density obtained by multiplying the measured IPCE by the spectral photon flux was integrated by wavelength to calculate the photocurrent density. The η_{sep} was calculated by dividing the sulfite oxidation current density measured in 1 M KOH with 0.2 M Na_2SO_3 by the absorption current density, which was calculated based on the UV-visible absorption spectrum. The EIS was measured from 100 kHz to 1 Hz with an amplitude of 10 mV and fitted with ZView software (Scribner Associates). Faradaic efficiencies at 1.23 V_{RHE} were calculated by the gas chromatography (7890B, Agilent Technologies) connected to an air-tight H-cell with the photoanode and Pt mesh. The M-S plots were obtained by the cathodic potential scan at a frequency of 1 kHz in a dark box. The OCP-derived carrier lifetimes were calculated by the time derivative of the OCP decay induced by blocked light after irradiation for 10 min. The *J–V* curves of the perovskite/Si solar cells and the 2-electrode cell comprising the $NiFeO_x$/CPF-TTB/Ta_3N_5/TiN photoanode and Pt cathode were measured under mode P, in which light was independently irradiated into the two light absorbers. The *J–t* curve of the tandem device, where the solar cell, photoanode, and cathode were connected by wires, was measured under the bias of 0 V. The STH conversion efficiency of the tandem device under mode P was calculated using the following equation:

$$STH\ (\%) = 0.5 \times J_{OP} \times 1.23 \times \eta_F / P_{in} \quad (7)$$

where J_{OP} is the operating photocurrent density (mA cm^{-2}) and η_F is the Faradaic efficiency.

DFT Calculations: The spin-polarized DFT calculations were performed using the Vienna Ab-initio Simulation Package with the projector augmented wave method for the core region and a plane-wave kinetic energy cutoff of 400 eV. The generalized gradient approximation in the form of Perdew-Burke-Ernzerhof for the exchange-correlation potentials was used. A 6 × 2 × 2 gamma-centered Monkhorst-pack sampled *k*-point grid was employed to sample the reciprocal space for the bulk Ta_3N_5. Monkhorst-pack *k*-point meshes of 2 × 2 × 1 were used for structure optimization and property calculation of Ta_3N_5 (110) slab, CPF-TTB, and the heterojunction CPF-TTB/Ta_3N_5 (110) heterostructure. The large vacuum layers of these slab models were set at least 15 Å in the *z*-direction for the isolation of the surface to prevent the interaction between two periodic units. The surface of Ta_3N_5 (110) was carried out using the slab model composed of $p(2 \times 2)$ supercells with four metal atomic monolayers. The bottom three atomic monolayers of Ta_3N_5 (110) were fixed at their bulk positions while the rest of atomic layers and 2D CPF-TTB layer were free to move in all directions until the convergence of energy and residual force on each atom were less than 1×10^{-4} eV and 0.05 eV $Å^{-1}$, respectively. To describe the charge transfer process in the CPF-TTB/Ta_3N_5 heterostructure, the dipole moment on the *z*-direction was calculated, and planar averaged charge density was acquired by averaging charge density on the *xy* plane toward the *z*-direction.

Supporting Information

Supporting Information is available from the Wiley Online Library or from the author.

Acknowledgements

This research was supported by the National Research Foundation of Korea (NRF) grant funded by the Korea government Ministry of Science and ICT (MSIT) (2021R1A2B5B03001851, 2021M3H4A1A03057403). This work was also supported by the KRISS (Korea Research Institute of Standards and Science) MPI Lab. program. H.W.J. gratefully acknowledges the KRISS MPI Lab. program. J.W.Y. acknowledges the NRF grant funded by the

Korea government MSIT (RS-2023-00213786). The Inter-University Semiconductor Research Center and Institute of Engineering Research at Seoul National University provided research facilities for this work.

Conflict of Interest

The authors declare no conflict of interest.

Data Availability Statement

The data that support the findings of this study are available in the supplementary material of this article.

Keywords

conjugated polymer, hole transport layer, tantalum nitride photoanodes, unbiased solar water splitting

Received: January 15, 2024
Revised: February 17, 2024
Published online:

[1] J. Lv, J. Xie, A. G. A. Mohamed, X. Zhang, Y. Feng, L. Jiao, E. Zhou, D. Yuan, Y. Wang, *Nat. Rev. Chem.* **2023**, *7*, 91.
[2] Q. Wang, C. Pornrungroj, S. Linley, E. Reisner, *Nat. Energy* **2022**, *7*, 13.
[3] M. Grätzel, *Nature* **2001**, *414*, 338.
[4] V. Andrei, G. M. Ucoski, C. Pornrungroj, C. Uswachoke, Q. Wang, D. S. Achilleos, H. Kasap, K. P. Sokol, R. A. Jagt, H. Lu, T. Lawson, A. Wagner, S. D. Pike, D. S. Wright, R. L. Z. Hoye, J. L. MacManus-Driscoll, H. J. Joyce, R. H. Friend, E. Reisner, *Nature* **2022**, *608*, 518.
[5] T. S. Teitsworth, D. J. Hill, S. R. Litvin, E. T. Ritchie, J. S. Park, J. P. Custer, A. D. Taggart, S. R. Bottum, S. E. Morley, S. Kim, J. R. McBride, J. M. Atkin, J. F. Cahoon, *Nature* **2023**, *614*, 270.
[6] R. T. Gao, N. T. Nguyen, T. Nakajima, J. He, X. Lu, X. Zhang, L. Wang, L. Wu, *Sci. Adv.* **2023**, *9*, eade4589.
[7] Z. W. She, J. Kibsgaard, C. F. Dickens, I. Chorkendorff, J. K. Nørskov, T. F. Jaramillo, *Science* **2017**, *355*, 146.
[8] A. Peugeot, C. E. Creissen, D. Karapinar, H. N. Tran, M. Schreiber, M. Fontecave, *Joule* **2021**, *5*, 1281.
[9] Z. Wang, Y. Inoue, T. Hisatomi, R. Ishikawa, Q. Wang, T. Takata, S. Chen, N. Shibata, Y. Ikuhara, K. Domen, *Nat. Catal.* **2018**, *1*, 756.
[10] H. R. Kwon, J. W. Yang, S. Choi, W. S. Cheon, I. H. Im, Y. Kim, J. Park, G. Lee, H. W. Jang, *Adv. Energy Mater.* **2023**, *14*, 2303342.
[11] P. Zhang, J. Zhang, J. Gong, *Chem. Soc. Rev.* **2014**, *43*, 4395.
[12] H. Hajibabaei, D. J. Little, A. Pandey, D. Wang, Z. Mi, T. W. Hamann, *ACS Appl. Mater. Interfaces* **2019**, *11*, 15457.
[13] J. W. Yang, S. H. Ahn, H. W. Jang, *Curr. Opin. Green. Sustain. Chem.* **2021**, *29*, 100454.
[14] P. Zhang, T. Wang, J. Gong, *Chem. Commun.* **2016**, *52*, 8806.
[15] Y. Zhao, H. Xie, W. Shi, H. Wang, C. Shao, C. Li, *J. Energy Chem.* **2022**, *64*, 33.
[16] M. Zhong, T. Hisatomi, Y. Sasaki, S. Suzuki, K. Teshima, M. Nakabayashi, N. Shibata, H. Nishiyama, M. Katayama, T. Yamada, K. Domen, *Angew. Chem.* **2017**, *129*, 4817.
[17] E. Nurlaela, Y. Sasaki, M. Nakabayashi, N. Shibata, T. Yamada, K. Domen, *J. Mater. Chem. A.* **2018**, *6*, 15265.
[18] Y. Pihosh, V. Nandal, T. Minegishi, M. Katayama, T. Yamada, K. Seki, M. Sugiyama, K. Domen, *ACS Energy Lett.* **2020**, *5*, 2492.
[19] Y. Hou, T. Li, S. Yan, Z. Zou, *Appl. Catal. B* **2020**, *269*, 118777.
[20] G. Liu, S. Ye, P. Yan, F. Xiong, P. Fu, Z. Wang, *Energy Environ. Sci.* **2016**, *9*, 1327.
[21] Y. Zhao, G. Liu, H. Wang, Y. Gao, T. Yao, W. Shi, C. Li, *J. Mater. Chem. A* **2021**, *9*, 11285.
[22] B. Zhang, Z. Fan, Y. Chen, C. Feng, S. Li, Y. Li, *Angew. Chem.* **2023**, *135*, e202305123.
[23] L. Pei, Z. Xu, Z. Shi, H. Zhu, S. Yan, Z. Zou, *J. Mater. Chem. A* **2017**, *5*, 20439.
[24] X. Zou, X. Han, C. Wang, Y. Zhao, C. Du, B. Shan, *Sustain. Energy Fuels* **2021**, *5*, 2877.
[25] Y. Xiao, Z. Fan, M. Nakabayashi, Q. Li, L. Zhou, Q. Wang, C. Li, N. Shibata, K. Domen, Y. Li, *Nat. Commun.* **2022**, *13*, 7769.
[26] Y. Li, L. Zhang, A. Torres-Pardo, J. M. González-Calbet, Y. Ma, P. Oleynikov, O. Terasaki, S. Asahina, M. Shima, D. Cha, L. Zhao, K. Takanabe, J. Kubota, K. Domen, *Nat. Commun.* **2013**, *4*, 2566.
[27] V. Nandal, Y. Pihosh, T. Higashi, T. Minegishi, T. Yamada, K. Seki, M. Sugiyama, K. Domen, *Energy. Environ. Sci.* **2021**, *14*, 4038.
[28] K. M. Coakley, M. D. McGehee, *Chem. Mater.* **2004**, *16*, 4533.
[29] S. Günes, H. Neugebauer, N. S. Sariciftci, *Chem. Rev.* **2007**, *107*, 1324.
[30] L. R. MacFarlane, H. Shaikh, J. D. Garcia-Hernandez, M. Vespa, T. Fukui, I. Manners, *Nat. Rev. Mater.* **2021**, *6*, 7.
[31] S. Y. Son, G. Lee, H. Wang, S. Samson, Q. Wei, Y. Zhu, W. You, *Nat. Commun.* **2022**, *13*, 2739.
[32] P. Patsalas, N. Kalfagiannis, S. Kassavetis, G. Abadias, D. V. Bellas, C. Lekka, E. Lidorikis, *Mater. Sci. Eng. R* **2018**, *123*, 1.
[33] S. Ye, V. Lotocki, H. Xu, D. S. Seferos, *Chem. Soc. Rev.* **2022**, *51*, 6442.
[34] R. D. McCullough, *Adv. Mater.* **1998**, *10*, 93.
[35] S. A. Lee, J. W. Yang, S. Choi, H. W. Jang, *Exploration* **2021**, *1*, 20210012.
[36] J. Roncali, *Chem. Rev.* **1992**, *92*, 711.
[37] M. Zhang, X. Jing, S. Zhao, P. Shao, Y. Zhang, S. Yuan, Y. Li, C. Gu, X. Wang, Y. Ye, X. Feng, B. Wang, *Angew. Chem.* **2019**, *131*, 8860.
[38] Y. Zheng, Y. Jiao, Y. Zhu, L. H. Li, Y. Han, Y. Chen, A. Du, M. Jaroniec, S. Z. Qiao, *Nat. Commun.* **2014**, *5*, 3783.
[39] J. Chen, C. L. Dong, D. Zhao, Y. C. Huang, X. Wang, L. Samad, L. Dang, M. Shearer, S. Shen, L. Guo, *Adv. Mater.* **2017**, *29*, 1606198.
[40] K. H. Ye, H. Li, D. Huang, S. Xiao, W. Qiu, M. Li, Y. Hu, W. Mai, H. Ji, S. Yang, *Nat. Commun.* **2019**, *10*, 3687.
[41] Y. Zhang, H. Lv, Z. Zhang, L. Wang, X. Wu, H. Xu, *Adv. Mater.* **2021**, *33*, 2008264.
[42] L. Wang, W. Lian, B. Liu, H. Lv, Y. Zhang, X. Wu, T. Wang, J. Gong, T. Chen, H. Xu, *Adv. Mater.* **2022**, *34*, 2200723.
[43] Y. Pihosh, V. Nandal, R. Shoji, R. Bekarevich, T. Higashi, V. Nicolosi, H. Matsuzaki, K. Seki, K. Domen, *ACS Energy Lett.* **2023**, *8*, 2106.
[44] Y. He, J. E. Thorne, C. H. Wu, P. Ma, C. Du, Q. Dong, J. Guo, D. Wang, *Chem* **2016**, *1*, 640.
[45] Y. He, P. Ma, S. Zhu, M. Liu, Q. Dong, J. Espano, X. Yao, D. Wang, *Joule* **2017**, *1*, 831.
[46] J. Fu, Z. Fan, M. Nakabayashi, H. Ju, N. Pastukhova, Y. Xiao, C. Feng, N. Shibata, K. Domen, Y. Li, *Nat. Commun.* **2022**, *13*, 729.
[47] M. Zhong, T. Hisatomi, Y. Kuang, J. Zhao, M. Liu, A. Iwase, Q. Jia, H. Nishiyama, T. Minegishi, M. Nakabayashi, N. Shibata, R. Niishiro, C. Katayama, H. Shibano, M. Katayama, A. Kudo, T. Yamada, K. Domen, *J. Am. Chem. Soc.* **2015**, *137*, 5053.
[48] R. T. Gao, J. Zhang, T. Nakajuma, J. He, X. Liu, X. Zhang, L. Wang, L. Wu, *Nat. Commun.* **2023**, *14*, 2640.
[49] R. T. Gao, L. Liu, Y. Li, Y. Yang, J. He, X. Liu, X. Zhang, L. Wang, L. Wu, *Proc. Natl. Acad. Sci. USA* **2023**, *120*, e2300493120.
[50] H. Zhang, D. Li, W. J. Byun, X. Wang, T. J. Shin, H. Y. Jeong, H. Han, C. Li, J. S. Lee, *Nat. Commun.* **2020**, *11*, 4622.
[51] Y. Lin, Y. Xu, M. T. Mayer, Z. I. Simpson, G. McMahon, S. Zhou, D. Wang, *J. Am. Chem. Soc.* **2012**, *134*, 5508.

[52] J. Fu, F. Wang, Y. Xiao, Y. Yao, C. Feng, L. Chang, C. M. Jiang, V. F. Kunzelmann, Z. M. Wang, A. O. Govorov, I. D. Sharp, Y. Li, *ACS Catal.* **2020**, *10*, 10316.
[53] M. G. Lee, J. W. Yang, H. Park, C. W. Moon, D. M. Andoshe, J. Park, C. K. Moon, T. H. Lee, K. S. Choi, W. S. Cheon, J. J. Kim, H. W. Jang, *Nano-Micro Lett.* **2022**, *14*, 48.
[54] S. R. Pendlebury, X. Wang, F. L.e Formal, M. Cornuz, A. Kafizas, S. D. Tilley, M. Grätzel, J. R. Durrant, *J. Am. Chem. Soc.* **2014**, *136*, 9854.
[55] W. Yang, S. Lee, H. C. Kwon, J. Tan, H. Lee, J. Park, Y. Oh, H. Choi, J. Moon, *ACS Nano* **2018**, *12*, 11088.
[56] J. W. Yang, I. J. Park, S. A. Lee, M. G. Lee, T. H. Lee, H. Park, C. Kim, J. Park, J. Moon, J. Y. Kim, H. W. Jang, *Appl. Catal. B* **2021**, *293*, 120217.
[57] M. G. Lee, J. W. Yang, I. J. Park, T. H. Lee, H. Park, W. S. Cheon, S. A. Lee, H. Lee, S. G. Ji, J. M. Suh, J. Moon, J. Y. Kim, H. W. Jang, *Carbon Energy* **2023**, *5*, e321.
[58] S. A. Lee, J. W. Yang, T. H. Lee, I. J. Park, C. Kim, S. H. Hong, H. Lee, S. Choi, J. Moon, S. Y. Kim, J. Y. Kim, H. W. Jang, *Appl. Catal. B* **2022**, *317*, 121765.
[59] K. Y. Yoon, J. Park, M. Jung, S. G. Ji, H. Lee, J. H. Seo, M. J. Kwak, S. I. Seok, J. H. Lee, J. H. Jang, *Nat. Commun.* **2021**, *12*, 4309.
[60] S. G. Ji, I. J. Park, H. Chang, J. H. Park, G. P. Hong, B. K. Choi, J. H. Jang, Y. J. Choi, H. W. Lim, Y. J. Ahn, S. J. Park, K. T. Nam, T. Hyeon, J. Park, D. H. Kim, J. Y. Kim, *Joule* **2022**, *6*, 2390.